Supplementary Information

Graphite carbon rings modified carbon nitride with strong built-in electric field for high photocatalysis-self-Fenton performance

Liang Jian[a#], Hui Zhao [a#], Yuming Dong [a, *], Jing Xu [b], Qinyi Mao[a], Rong Ji [a], Zhuying Yan [b], Chengsi Pan[a], Guangli Wang[a], Yongfa Zhu[c, a]

[a] International Joint Research Center for Photo-responsive Molecules and Materials, School of Chemical and Material Engineering, Jiangnan University, Wuxi, 214122, China.

[b] State Key Laboratory of Food Science and Technology, Jiangnan University, Wuxi, 214122, China.

[c] Department of Chemistry, Tsinghua University, Beijing, 100084, China.

[#] Equal contribution

* Corresponding authors: Prof. Yuming Dong: dongym@jiangnan.edu.cn

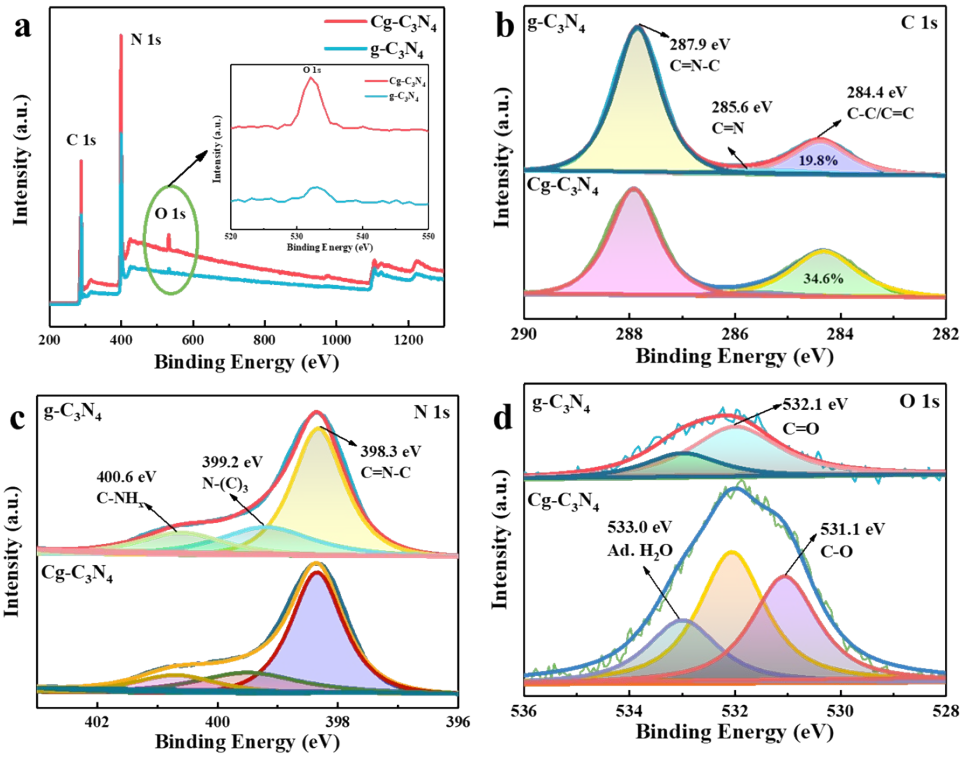

Figure S1 (a) The XPS spectra of g-C_3N_4 and Cg-C_3N_4; (b) and (c) The C 1s, N 1s, and O1 s high-resolution XPS spectra of g-C_3N_4 and Cg-C_3N_4.

To analyze their compositions, the XPS indicate the O 1s, N 1s, and C 1s peak of Cg-C_3N_4 and g-C_3N_4 (Fig. S1a). All data for XPS were calibrated by the C-1s calibration peak as reference (284.6 eV). The N 1s high-resolution XPS spectra (Fig. S1c) show that the dominant peak at 398.3 eV, 399.2 eV, and 400.6 eV were ascribed to hybridized sp^2 aromatic N (C-N=C), bridging tertiary N peak (N-$(C)_3$) and amino functional groups (C-NH_2), respectively. Next, the high-resolution O 1s XPS spectrum of Cg-C_3N_4 is investigated (Fig. S1d). Apparently, in contrast to g-C_3N_4, a new peak appeared at about 531.1 eV in Cg-C_3N_4 that is assigned to the uncondensed C−O in 1,3,5-cyclohexanetriol. The peak at 533.0 eV corresponds to the adsorbed water molecules on the g-C_3N_4 surface, and the peak at 532.1 eV is assigned to the partial condensed C=O containing urea [52].

Table S1 The elemental composition (%) and the atomic ratio of C, N, O in Cg-C_3N_4 and g-C_3N_4 measured by XPS

XPS	C/%	N/%	O/%	C/N
Cg-C_3N_4	46.21	51.17	2.62	0.90
g-C_3N_4	43.40	55.08	1.52	0.79

Table S2 The elemental composition (%) and the atomic ratio of C, N, O in Cg-C_3N_4 and g-C_3N_4 were measured by elemental analysis

Elemental Analysis	C/%	N/%	O/%	C/N
Cg-C_3N_4	32.17	57.39	8.124	0.56
g-C_3N_4	33.01	60.41	5.02	0.55

The elemental composition was measured by XPS. As shown in Table S1, the C/N atomic ratio of Cg-C_3N_4 was 0.90 relative to the C/N atomic ratio of g-C_3N_4 (0.79). Meanwhile, the C/N atomic ratios of g-C_3N_4 and Cg-C_3N_4 were measured by elemental analysis to be 0.55 and 0.56, respectively, indicating the incorporation of additional carbon into the graphitic carbon nitride. In addition, the elemental analysis shows that the O content of Cg-C_3N_4 is 8.12%, which is higher than that of g-C_3N_4. It is illustrated that the introduction of oxygen-containing groups leads to an increase in oxygen content.

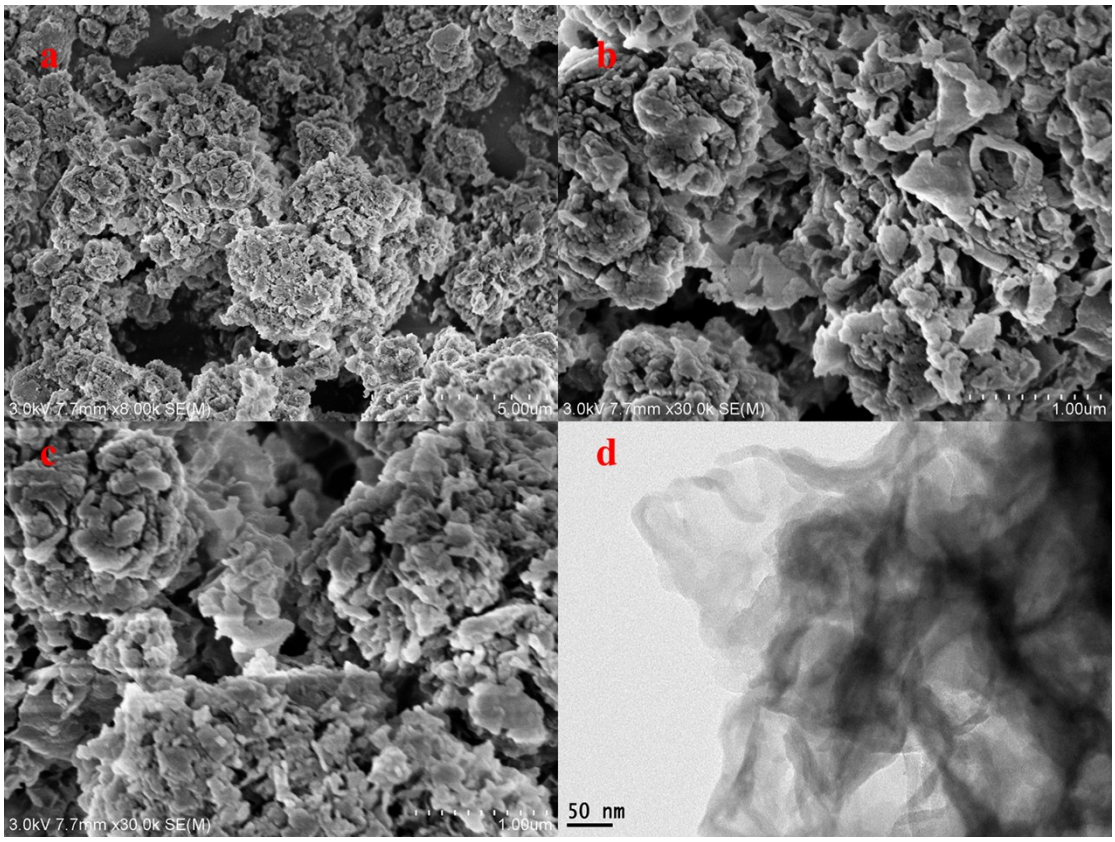

Figure S2 (a), (b), and (c) The SEM images of Cg-C_3N_4; (d) The TEM images of Cg-C_3N_4.

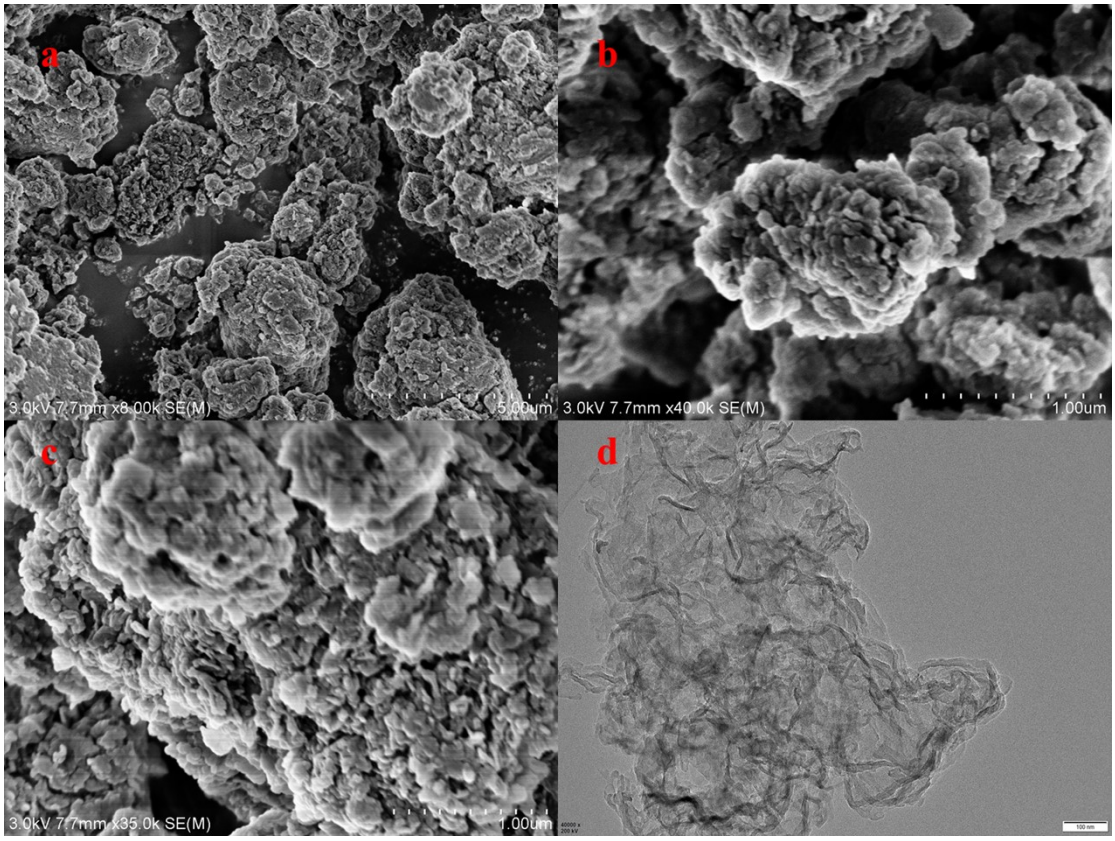

Figure S3 (a), (b), and (c) The SEM images of g-C_3N_4; (d) The TEM images of g-C_3N_4.

The nanostructures of pristine g-C_3N_4 are shown in Figure S3. Figure S2 shows the packing structure of Cg rings doped carbon nitride nanosheets.

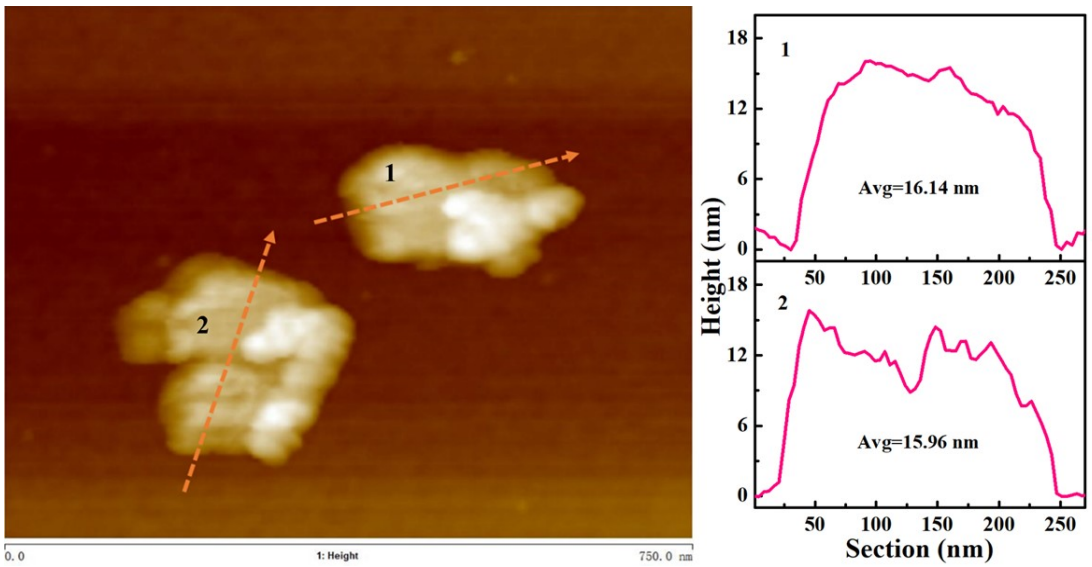

Figure S4 The atomic force microscopy (AFM) image and average thickness distribution of Cg-C_3N_4.

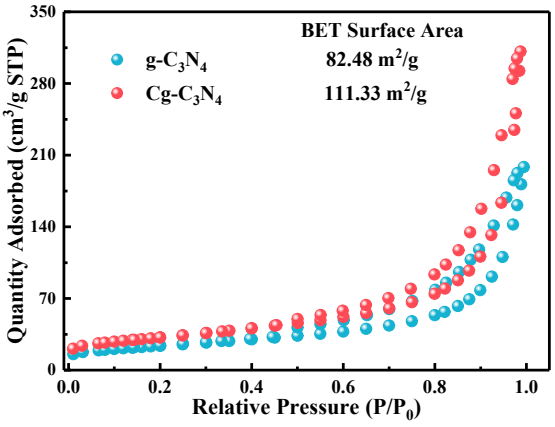

Figure S5 N_2 adsorption-desorption isotherms for g-C_3N_4 and Cg-C_3N_4.

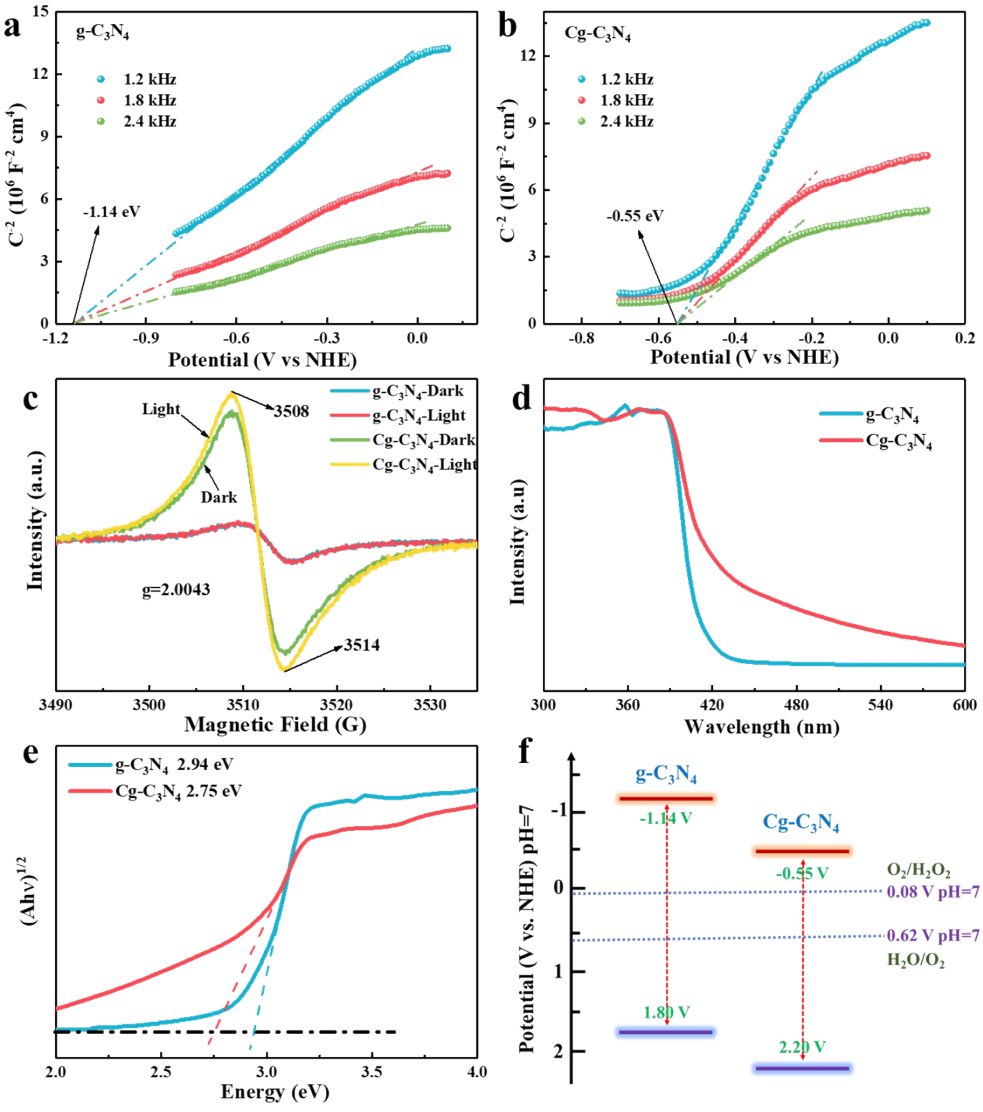

Figure S6 The Model Schottky curves of (a) g-C_3N_4 and (b) Cg-C_3N_4 at selected frequencies of 1.2, 1.8, and 2.4

kHz; (c) The EPR spectra of g-C_3N_4 and Cg-C_3N_4 in the dark and under visible light (λ > 420 nm), respectively; (d) The diffuse reflectance UV spectrum of g-C_3N_4 and Cg-C_3N_4; (e) The Tauc curve and (f) band gap structure of g-C_3N_4 and Cg-C_3N_4.

As shown in Figures S5a and S5b, g-C_3N_4 and Cg-C_3N_4 are the typical n-type semiconductor. The band edge positions of g-C_3N_4 and Cg-C_3N_4 can be calculated using the following equation:

$$E_{CB} = (V\ vs.\ NHE) = E_{fb}(V\ vs.\ AgCl/Ag) + 0.197 - X \text{------Eq. s1}$$

$$E_{VB} = E_{CB} + E_g \text{------ Eq. s2}$$

Where E_{VB} and E_{CB} stand for the valence band edge potential and conduction band edge potential, respectively; $E_{Ag/AgCl}$=0.197V (saturated potassium chloride) vs. NHE; X is the voltage difference between the conduction band value and the flat potential value, generally 0.1-0.2 eV (the conduction bands of n-type semiconductors are normally 0.1-0.2 eV deeper than the flat-band potential), which is set as 0.2 eV in this work. The E_{CB} of g-C_3N_4 and Cg-C_3N_4 are -1.14 and -0.55 eV (vs. NHE), respectively; the E_{VB} are 1.80 and 2.20 eV (vs. NHE), respectively.

Meanwhile, the doping of Cg rings changes the electron paramagnetic resonance of the material. The g-C_3N_4 and Cg-C_3N_4 show one single Lorentzian line with a g value of 2.0043, which is attributed to an unpaired electron on the carbon atoms of the aromatic rings within the π-bonded nanoclusters (Fig. S5c). The strong electron paramagnetic resonance signal of Cg-C_3N_4 indicates the larger electron density. When Cg-C_3N_4 was irradiated with visible light, the enhancement of the EPR signal was further observed, indicating efficient photochemical generation of radical pairs in the semiconductor. The incorporation of Cg rings into g-C_3N_4 modifies the π-electron delocalization in the conjugated system, and thus changes the intrinsic optical/electronic properties of the resulting Cg-C_3N_4 polymers [45]. Therefore, the diffuse reflectance ultraviolet spectrum (Fig. S5d) shows that Cg-C_3N_4 exhibits a broad visible light response. Cg-C_3N_4 showed the narrow band gap obtained by the Tauc curve (Fig. S5e). As shown in Figure S5f, Cg-C_3N_4 has the corrected valence band position calculated by the model Schottky curve.

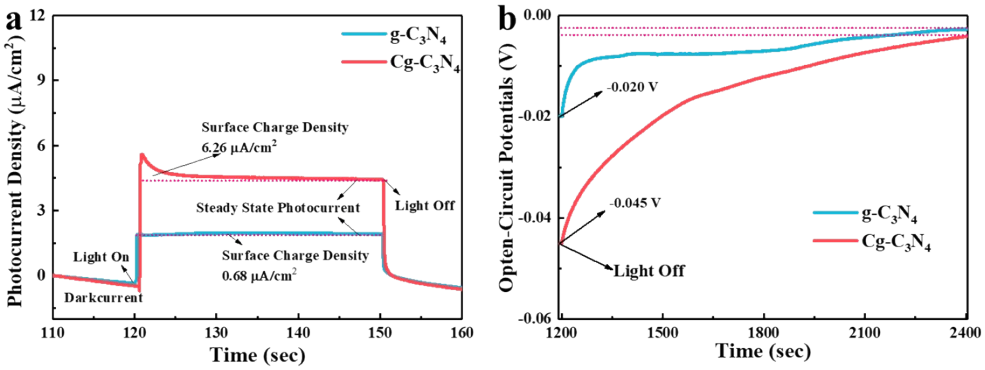

Figure S7 (a) and (b) Transient photocurrent density and open-circuit voltage of g-C_3N_4 and Cg-C_3N_4, respectively.

The built-in electric field (IEF) magnitude of g-C_3N_4 and Cg-C_3N_4 were calculated by using the following Eq. s3 reported by Kanata et al [S27-30]. It can be found that the IEF of Cg-C_3N_4 is 4.7 times as high as that of g-C_3N_4.

$$Fs=(-2V_s\rho/\varepsilon\varepsilon_0)^{1/2}\text{------Eq. s3}$$

Where Fs is the internal electric field magnitude, V_s is the surface voltage, ρ is the surface charge density, Ɛ is the low-frequency dielectric constant, and $Ɛ_0$ is the permittivity of free space. The above equation reveals that the internal electric field magnitude is mainly determined by the surface voltage and the charge density because Ɛ and $Ɛ_0$ are two constants. To evaluate the internal electric field magnitude of g-C_3N_4 and Cg-C_3N_4, we carefully figured out their charge densities by the transient photocurrent density measurements and surface voltages by open-circuit potentials measurements, which are shown in Figure S6a and Figure S6b, respectively. Le Formal and Gratzel et al. have reported that, by integrating the measured transient photocurrent density minus the steady state values of photocurrent concerning time, the value is proportional to the number of positive charges accumulated at the surface [S31]. Here, we measure the transient photocurrent and integrate the transient anodic photocurrent peaks. The surface charge density of g-C_3N_4 and Cg-C_3N_4 is shown in Figure S6a.

Table S3 Zeta potential (mV) of g-C_3N_4 and Cg-C_3N_4

Samples	Zeta-1	Zeta-2	Zeta-3	Zeta-4	Zeta-5	Zeta-AVG
Cg-C_3N_4	-16.41	-15.70	-17.99	-18.82	-15.57	-16.90
g-C_3N_4	-3.33	-1.56	-3.36	-6.49	-4.94	-3.94

According to Zhang et al. [S32-33], the built-in electric field is a monotonic function of the surface charge density and Zeta potential of a given material, so the built-in electric field can be represented by the Zeta potential. As shown in the table above, the average Zeta potential of Cg-C_3N_4 was −16.90 mV, which was 4.3 times higher than that of g-C_3N_4 (−3.94 mV).

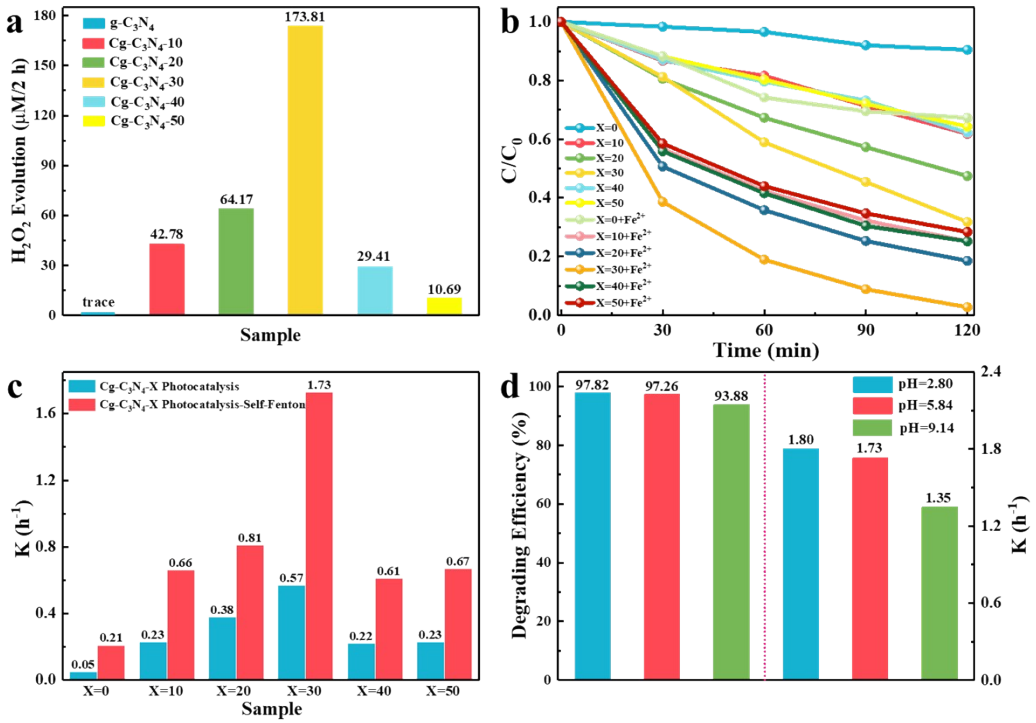

Figure S8 (a) The effect of the additional amount of 1,3,5-cyclohexanetriol on the photocatalytic H_2O_2 production of Cg-C_3N_4 in presence of the 4-chlorophenol (visible light λ>420 nm); (b) and (c) The effect of the addition amount of 1,3,5-cyclohexanetriol on the photocatalytic degradation performance of 4-chlorophenol (visible light λ>420 nm), corresponding the degradation curves and apparent degradation rate constants of photocatalytic and photocatalysis-self-Fenton, respectively; (d) The degradation efficiency and apparent degradation rate constant of photocatalysis-self-Fenton for the degradation of 4-chlorophenol at different pH values.

The aromatic carbocyclic doped graphitic carbon nitride (Cg-C_3N_4) was obtained by thermal polymerization of 1,3,5-cyclohexanetriol and urea mixture. When the added amount of 1,3,5-cyclohexanetriol was 30 mg (Fig. S8a-c), Cg-C_3N_4-based photocatalysis and photocatalysis-self-Fenton exhibited the best degradation activities, and Cg-C_3N_4 displays the best photocatalytic activity for H_2O_2 generation.

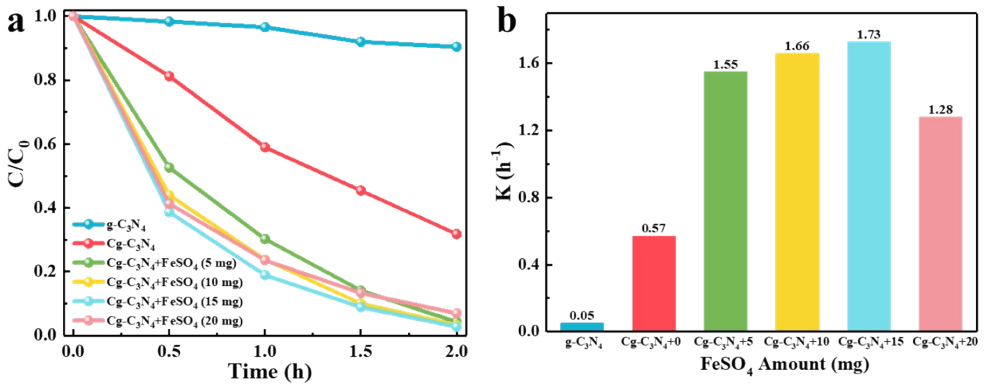

Figure S9 (a) The effect of $FeSO_4$ addition for the photocatalysis-self-Fenton degradation of 4-chlorophenol (visible light λ>420 nm), (b) Corresponding the apparent degradation rate constants for the photocatalytic and photocatalysis-self-Fenton degradation, respectively.

In addition to being highly dependent on the content of H_2O_2 in the photocatalysis-self-Fenton system, as shown in figures S9a and S9b, the additional amount of Fe^{2+} is equally important to the photocatalysis-self-Fenton system. When the dosage of the Fenton reagent was 15 mg, it showed the best degradation performance and degradation rate.

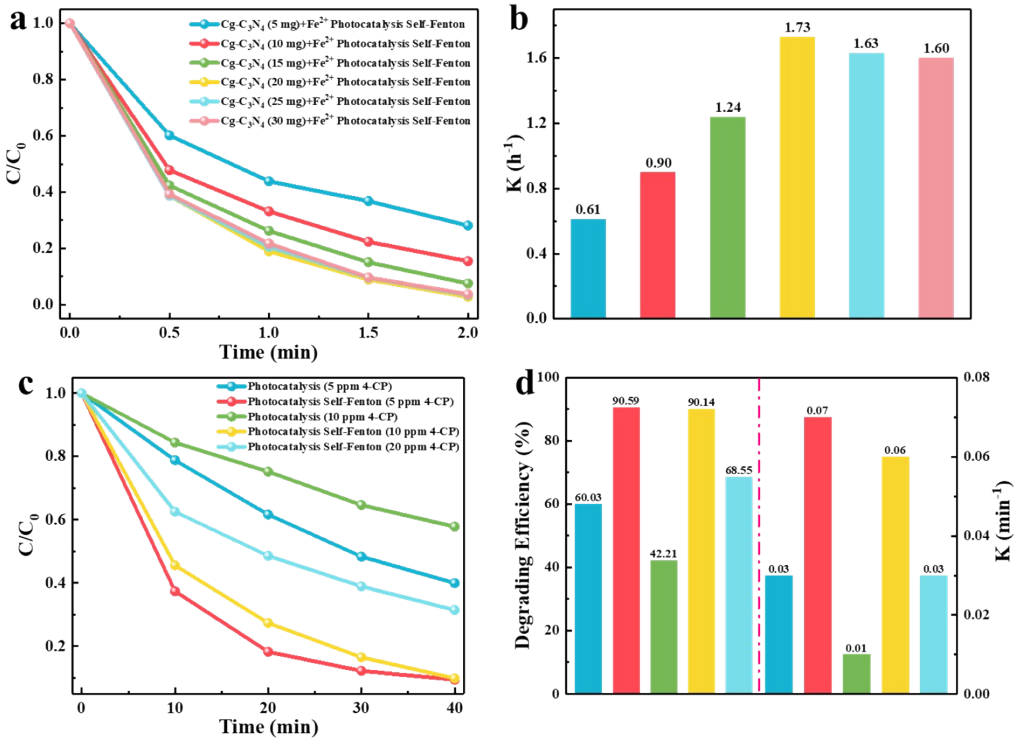

Figure S10 (a) and (b) The effect of photocatalyst dosage and the corresponding degradation curve and degradation rate constant of photocatalysis-self-Fenton degradation of 4-chlorophenol; (c) The degradation curves of photocatalytic and photocatalysis-self-Fenton under visible light (λ>420 nm) for different concentrations of 4-chlorophenol, and (d) corresponding degradation efficiencies and apparent degradation rate constants.

In the optimization of the amount of Photocatalyst (Fig. S10a, S10b), when the amount of photocatalyst is 20 mg, the photocatalysis-self-Fenton degradation activity, and degradation rate are optimal. Meanwhile, the photocatalysis-self-Fenton system exhibited high degradation rates and removal efficiencies for different concentrations of 4-chlorophenol (Fig. S10c and S10d).

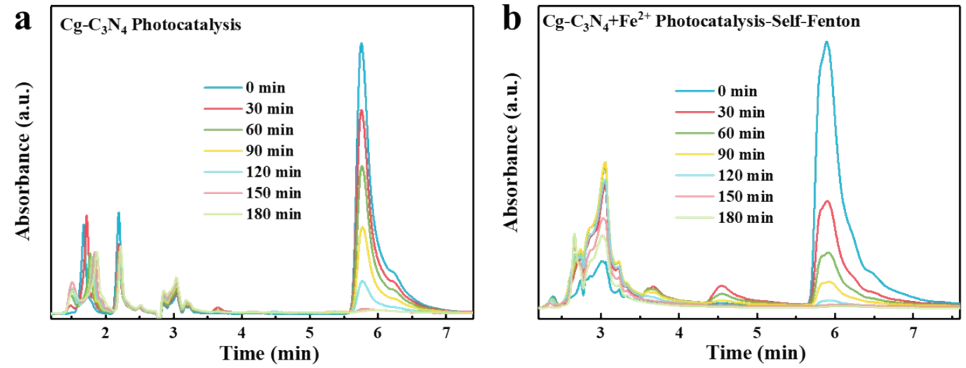

Figure S11 (a) and (b) correspond to the UHPLC degradation curves of photocatalytic and photocatalysis-self-Fenton degradation of 4-chlorophenol, respectively.

The photocatalysis-self-Fenton degradation curve (Fig. S11b) showed that the peak of the intermediate product decreased significantly after the reaction for 120 min, indicating that the photocatalysis-self-Fenton system has the ability to continuous degradation and mineralization ability.

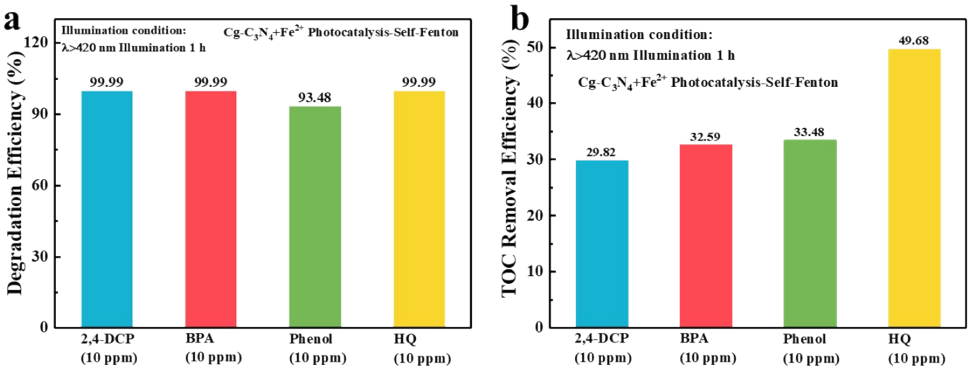

Figure S12 (a) The degradation efficiency with different organic pollutants (concentration: 10 ppm) under visible light (λ>420 nm); (b)The TOC removal efficiency of photocatalytic for different organic pollutants (concentration: 10 ppm) under visible light (λ>420 nm) for 1 hour of reaction.

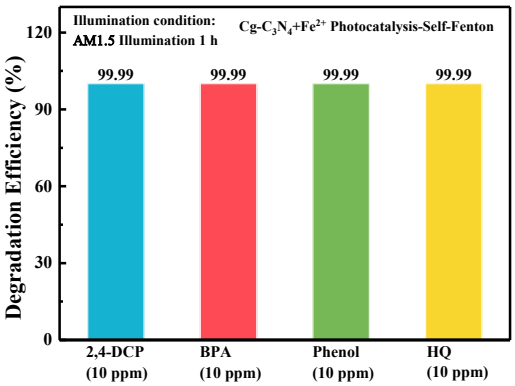

Figure S13 The degradation efficiency with different organic pollutants (concentration: 10 ppm) under the simulated sunlight (AM1.5).

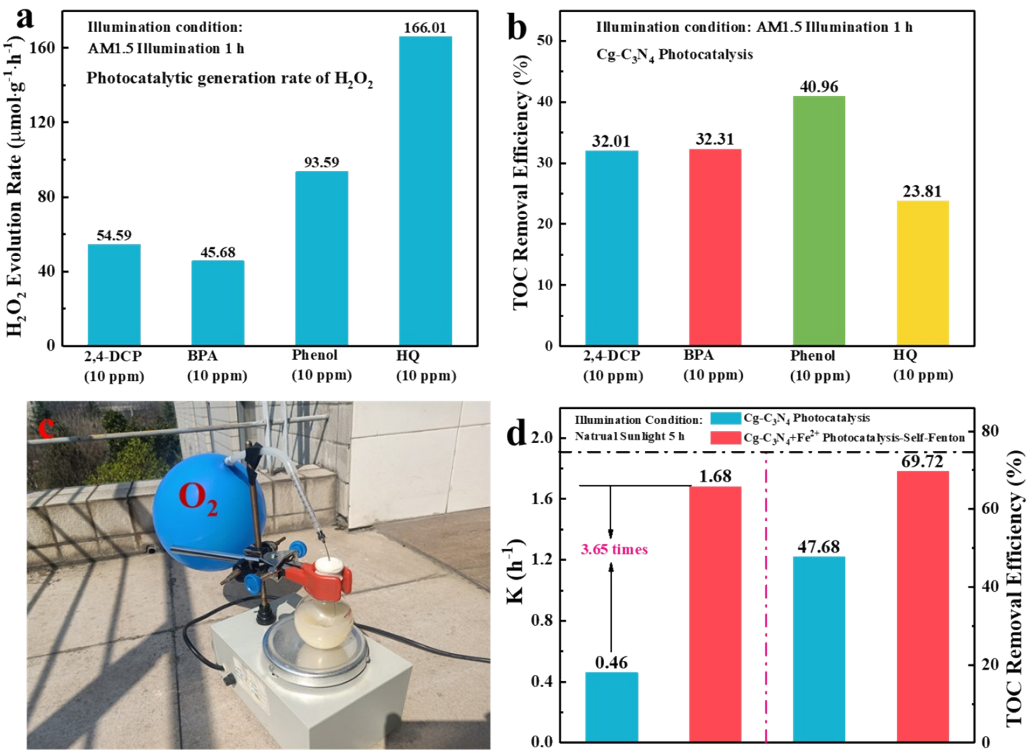

Figure S14 (a) Photocatalytic generation rate of H_2O_2 with different organic pollutants as sacrificial agents (concentration: 10 ppm) under the simulated sunlight (AM1.5); (b)The TOC removal efficiency of photocatalytic for different organic pollutants (concentration: 10 ppm) under the simulated sunlight (AM1.5) for 1 hour of reaction; (c) The actual pictures for photocatalysis-self-Fenton degradation of 4-chlorophenol under natural sunlight; (d) The photocatalytic and photocatalysis-self-Fenton degradation performance and TOC removal efficiency for 4-Chlorophenol (concentration: 20 ppm) under natural sunlight (continuous reaction for 5 h).

$Cg\text{-}C_3N_4$ exhibited efficient photocatalytic H_2O_2 production performance in presence of other

phenolic pollutants (Fig. 14a). Meanwhile, Cg-C_3N_4-based photocatalysis exhibits efficient TOC removal efficiency (Fig. 14b) under simulated sunlight (AM1.5) for 1 hour of reaction. Meanwhile, the rapid degradation of 4-chlorophenol can be achieved under natural sunlight (Fig. S14c and 14d). Under natural sunlight, the photocatalysis-self-Fenton system exhibits a degradation rate constant of 1.68 h^{-1}, and the TOC removal efficiency after the reaction for 5 hours reached 69.7 %, which are 3.65 times and 1.5 times that of the photocatalytic system, respectively (Fig. S14d).

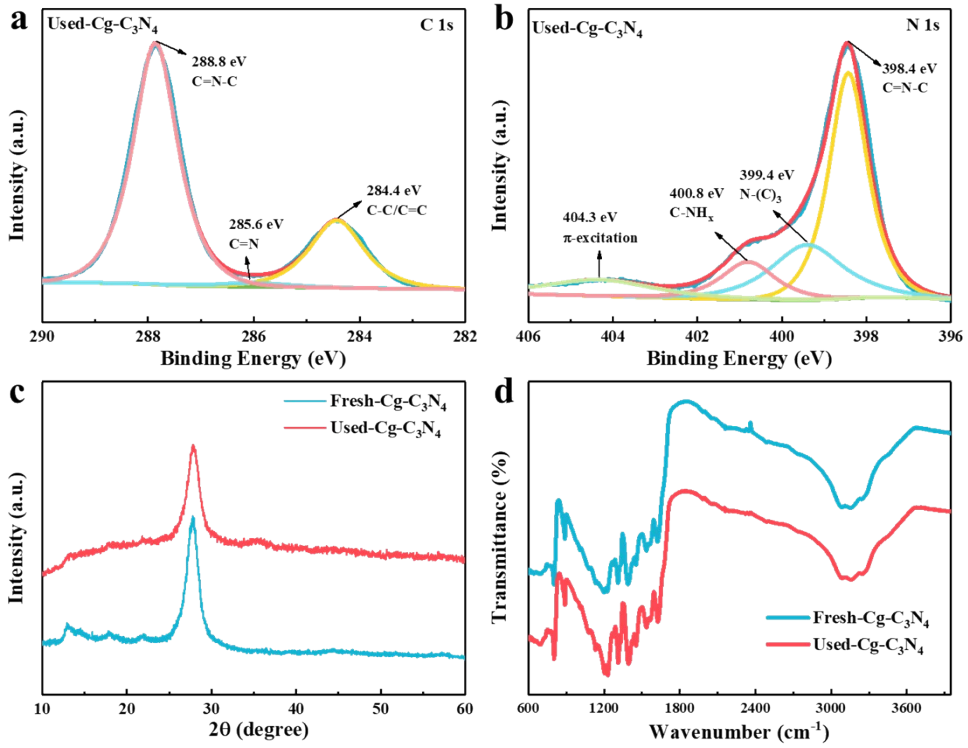

Figure S15 (a) and (b) The C 1s and N 1s high-resolution XPS spectra of Cg-C_3N_4 after the reaction; (c) The XRD spectra of Cg-C_3N_4 before and after the reaction; (d) The infrared spectra of Cg-C_3N_4 before and after the reaction.

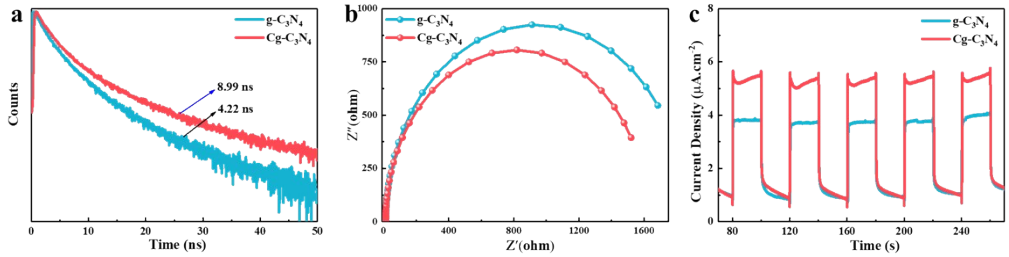

Figure S16 (a) Ultrafast time-resolved fluorescence lifetime spectra of g-C_3N_4 and Cg-C_3N_4; (b) The electrochemical impedance spectra of g-C_3N_4 and Cg-C_3N_4; (c) Transient surface photocurrents of g-C_3N_4 and Cg-C_3N_4.

The ultrafast time-resolved fluorescence spectroscopy (Fig. S16a) shows that Cg-C_3N_4 has a slower lifetime decay. The average decay lifetimes of g-C_3N_4 and Cg-C_3N_4 were calculated to be 4.22 ns and 8.99 ns by fitting the decay kinetics, respectively, indicating that the recombination of

photogenerated electrons and holes of Cg-C_3N_4 can be effectively suppressed. In addition, the electrochemical impedance spectroscopy (Fig. S16b) shows that Cg-C_3N_4 has a smaller EIS arc radius, further indicating the rapid migration and separation of photogenerated charges. The photocurrent response can be used to study the photogenerated carrier transfer efficiency and separation efficiency of Cg-C_3N_4. The higher the photo-generated carrier transfer efficiency and separation efficiency, the higher the photocurrent can be exhibited by the photocatalyst. As shown in Figure S16c, Cg-C_3N_4 exhibits higher photocurrent relative to g-C_3N_4.

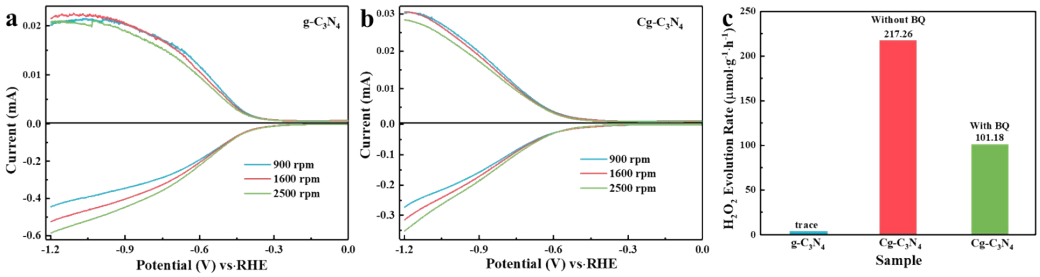

Figure S17 (a) and (b) correspond to the RRDE polarization curves of g-C_3N_4 and Cg-C_3N_4 coated electrodes, respectively, experimental conditions: carried out at different speeds (ω=900, 1600, and 2500 rpm) in O_2-saturated phosphate buffer solution (0.1 M pH=6.9) at room temperature; (c) The effect of p-benzoquinone (0.2 mM) as the superoxide radical scavenger on the photocatalytic H_2O_2 production rate.

As shown in Figures S17a and S17b, the RRDE polarization curves on g-C_3N_4 and Cg-C_3N_4-coated electrodes at different rotation numbers were measured. The reduction disc current (I_d) increases with the increase of the number of revolutions. As shown in Figure S12c, when g-C_3N_4 was used as the photocatalyst, only a small amount of H_2O_2 was generated. However, when Cg-C_3N_4 was used as the photocatalyst, the photocatalytic production rate of H_2O_2 reached 217.3 $\mu mol \cdot g^{-1} \cdot h^{-1}$. In addition, when p-benzoquinone was used as the superoxide radical scavenger, the photocatalytic generation rate of H_2O_2 was significantly inhibited (Fig. S17c). It shows that the superoxide radical is the intermediate product for the generation of H_2O_2.

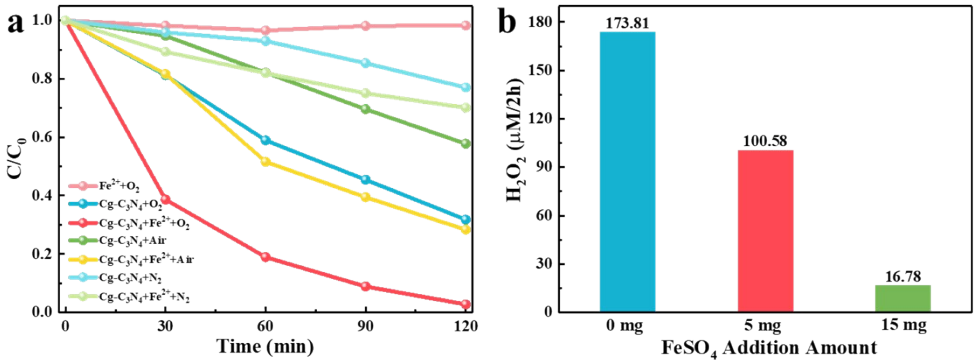

Figure S18 (a) The photocatalytic and photocatalysis-self-Fenton degradation activities under controlled

experimental conditions; (b) H_2O_2 accumulation detected after adding different amounts of ferrous sulfate.

As shown in Figure S18a, with the absence of a photocatalyst, 4-chlorophenol is very stable under visible light. Under an N_2 atmosphere, the photocatalysis-self-Fenton degradation rate constant (k value) is 0.18 h^{-1}, mainly due to the limited photocatalytic degradation activity. In the air and O_2 atmospheres without Fe^{2+}, the k values reach 0.28 h^{-1} and 0.57 h^{-1}, respectively, which are mainly attributed to the capture of electrons by O_2 to enhance the separation of photogenerated charges, thereby enhancing the photocatalytic degradation activity. In the air and O_2 atmospheres with the presence of Fe^{2+}, the k values increased to 0.65 h^{-1} and 1.73 h^{-1}, respectively, which were mainly due to the continuous generation of hydroxyl radicals, to improve the degradation activity. It shows that the Cg-C_3N_4 photocatalyst is the necessary factor to realize the degradation. Meanwhile, the degradation activities under different atmospheres showed that the main active species originate from O_2 and holes. As shown in Figure S18b, only a trace amount of H_2O_2 was detected after adding 15 mg of ferrous sulfate, indicating that the addition of Fe^{2+} promoted the decomposition of H_2O_2.

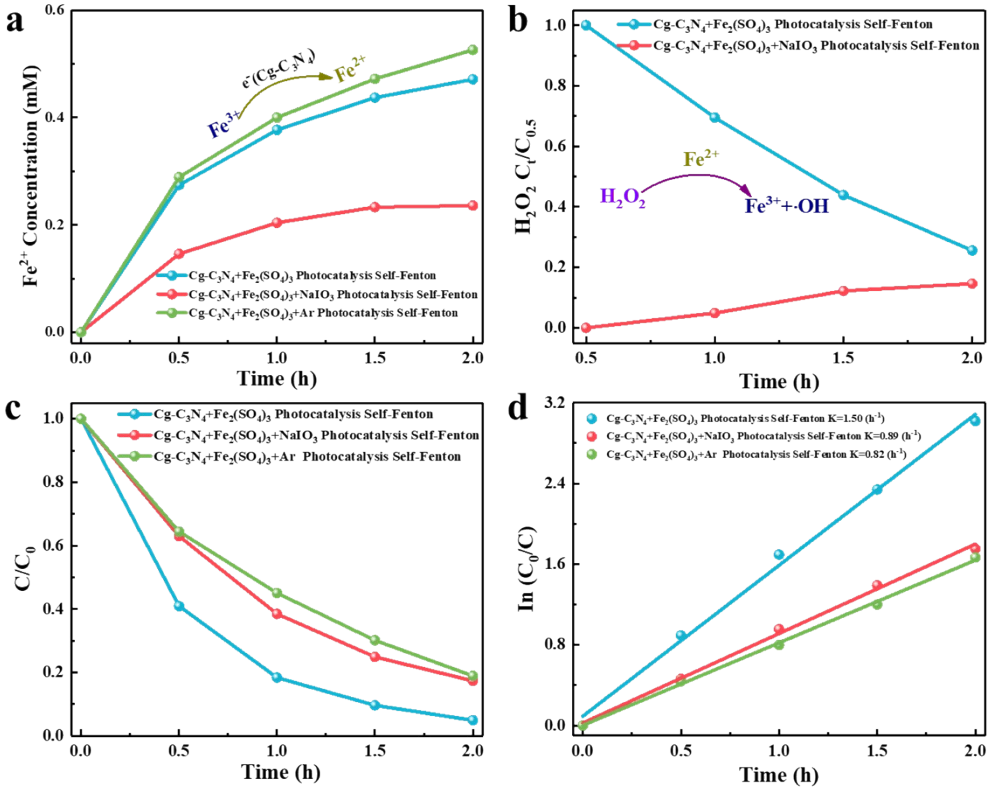

Figure S19 (a) and (b) the changes of Fe^{2+} concentration and H_2O_2 concentration detected in the solution when ferric sulfate was used as the Fenton reagent, respectively; (c) and (d) corresponding to the degradation activity and the fitting curves of apparent degradation rate when iron sulfate was used as the Fenton reagent, respectively.

The photocatalysis-self-Fenton degradation of 4-chlorophenol was constructed using ferric sulfate as the Fenton reagent (Fig. S19a). The efficient conversion of Fe^{3+} to Fe^{2+} promotes the decomposition of H_2O_2 to generate •OH radicals. At the same time, the transfer of photogenerated

holes is also promoted, resulting in the mineralization and rapid degradation of 4-chlorophenol with the apparent rate constant of 1.50 h^{-1} (Fig. S19b). The addition of a $NaIO_3$ electron capture agent inhibited the degradation activity and only a small amount of H_2O_2 concentration was detected. It shows that the addition of $NaIO_3$ electron capture agent not only inhibits the formation of H_2O_2 but also inhibits the photocatalysis-self-Fenton degradation activity (Fig. S19c and S19d). It further illustrates the effective conversion between Fe^{2+} and Fe^{3+} in the photocatalysis-self-Fenton system.

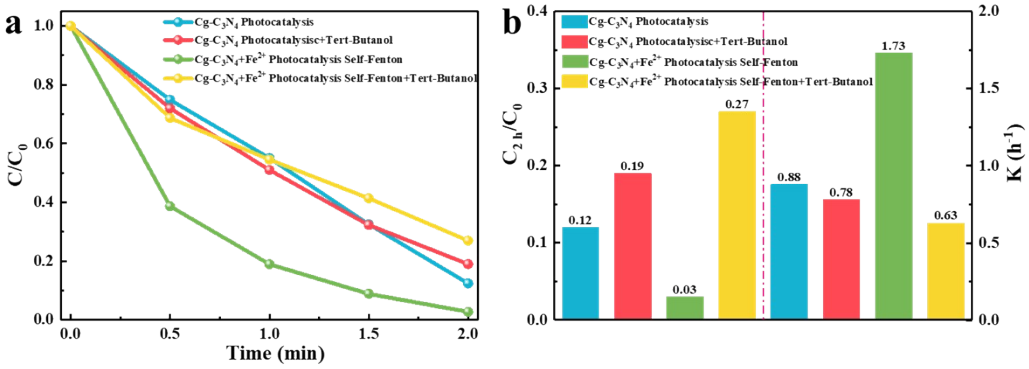

Figure S20 (a) and (b) The degradation activity and apparent degradation rate constants for hydroxyl radical (•OH) trapping experiments.

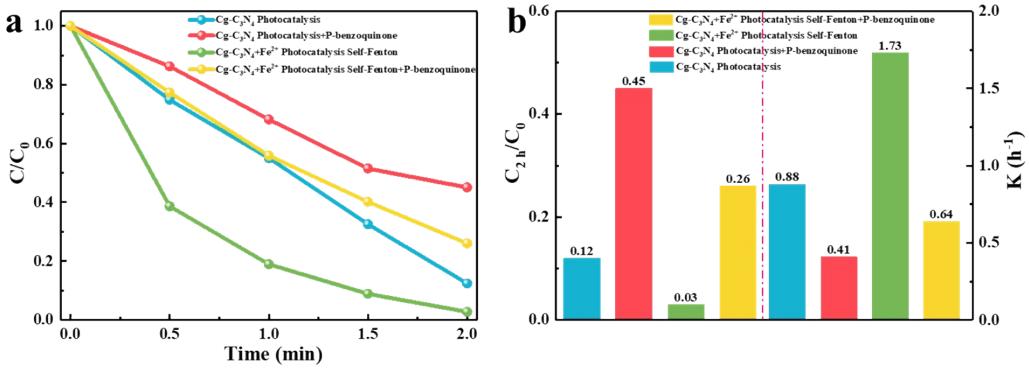

Figure S21 (a) and (b) The degradation activity and apparent degradation rate constants of superoxide radical ($•O_2^-$) capture experiments.

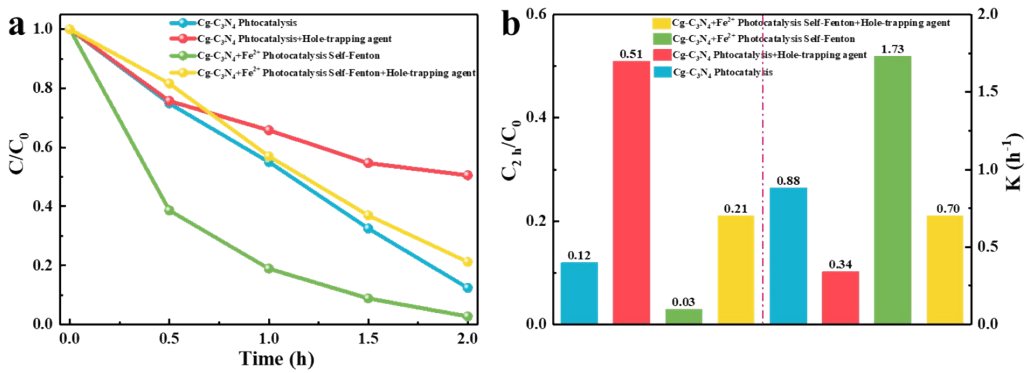

Figure S22 (a) and (b) The degradation activity and apparent degradation rate constants for the hole (h^+) trapping experiments.

As shown in Figure S20, when tert-butanol was used as the hydroxyl radical scavenger, it had little effect on the degradation rate of the photocatalytic system. However, when tert-butanol was added, the degradation rate of the photocatalysis-self-Fenton system was significantly inhibited. It is further demonstrated that hydroxyl radical is one of the main active species in the photocatalysis-self-Fenton system. The superoxide radical capture experiment (Fig. S21) showed that the addition of the capture agent significantly inhibited the degradation rates of the two systems. In addition, the hole-trapping experiments (Fig. S22) showed that the addition of hole-trapping agents significantly inhibited the degradation rates of both systems. It is further explained that the main active species in photocatalysis are superoxide radicals and holes, while the main active species in the photocatalysis-self-Fenton system are hydroxyl radicals, superoxide radicals, and holes.

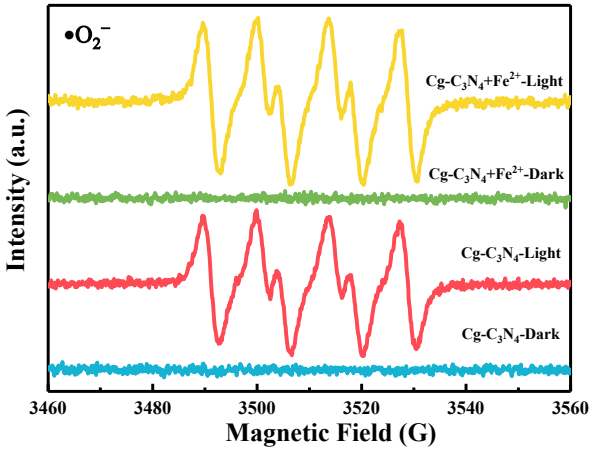

Figure S23 The electron spin-resonance spectroscopy spectra of superoxide radical ($•O^{2-}$) of Cg-C_3N_4.

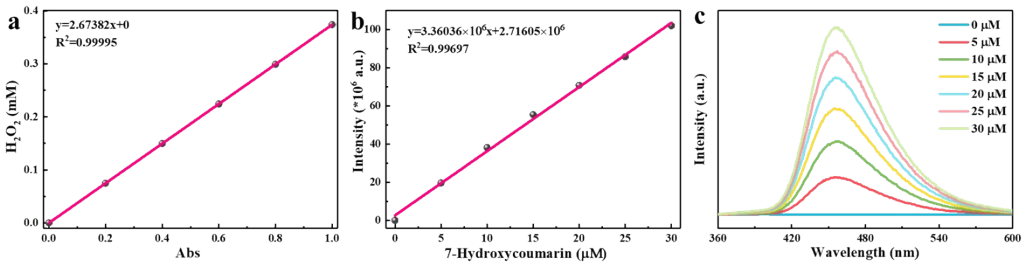

Figure S24 (a) The standard curve of H_2O_2; (b) The standard curve and (c) PL spectrum of 7-hydroxycoumarin.

The concentration of H_2O_2 was determined by UV-Vis spectrophotometer (JINGHUA, 200333) (S24a). The potassium titanium oxalate solution is used as the color developer for H_2O_2 [54]. Briefly, 3 mL of the sample solution was collected into the plastic centrifuge tube (10 mL), followed by the addition of 2 mL of potassium titanium oxalate solution (0.5 M). After shaking and stabilizing for 6-8 min, the absorbance of the mixed solution was measured at the wavelength of 400 nm. The linear relationship (R^2) of the resulting standard curve was 0.99995. The reaction of hydroxyl radicals with coumarin finally produced 7-hydroxycoumarin with fluorescent properties (Fig. S24c) [56]. The concentration of 7-hydroxycoumarin was determined by using the fluorescence spectrometer (FS5) with an excitation wavelength of 350 nm and an emission wavelength of 450 nm. The linear relationship (R^2) of the resulting standard curve was 0.99697 (Figure S24b).

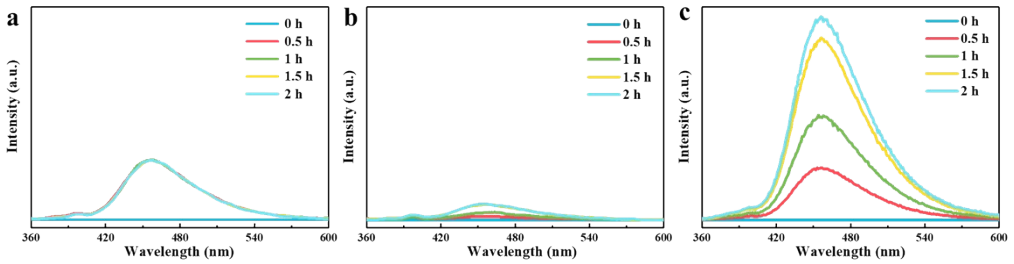

Figure S25 (a), (b), and (c) PL intensities of 7-hydroxycoumarins in Fenton, photocatalysis, and photocatalysis-self-Fenton.

The photoluminescence intensity of 7-hydroxycoumarin in the photocatalytic system, the Fenton system, and the photocatalysis-self-Fenton system was measured by fluorescence spectrometer, as shown in Figure S25. The corresponding concentration of 7-hydroxycoumarin was determined according to the linear equation in Figure S24b. The quantification of ·OH was measured by a fluorescence method [56], where the coumarin was used as a probe to determine the amount of ·OH generated during reactions. 6.1% of •OH can be detected as 7-hydroxycoumarin (umbelliferon) by 0.1 mM coumarin. Therefore, the •OH transformation efficiency of the photocatalysis-self-Fenton system and Fenton system is calculated as follows:

$$\bullet OH\ transformation\ efficiency\ (photocatalysis\ -\ self\ -\ Fenton) = \frac{\bullet OH\ (Concentration)}{H_2O_2\ (Total\ Concentration)} \approx 64.7\%$$

$$\bullet OH\ transformation\ efficiency\ (Fenton) = \frac{\bullet OH\ (Concentration)}{H_2O_2\ (Total\ Concentration)} \approx 7.69\%$$

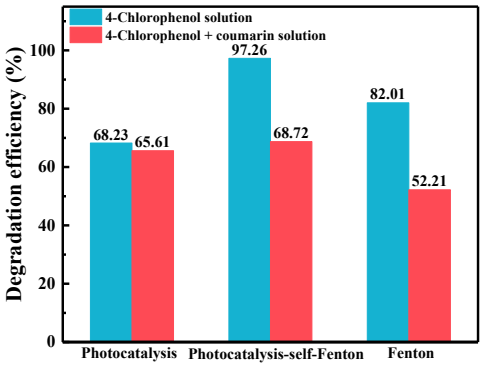

Figure S26 The degradation performance of 4-chlorophenol during the detection of hydroxyl radical concentration.

The concentration of •OH is detected by measuring the PL radiation signal intensity of 7-hydroxycoumarin, in which coumarin is used as the capture agent of •OH[56]. As shown in Figure S26, when coumarin was added to the reaction solution, the photocatalysis-self-Fenton and Fenton degradation properties were inhibited relative to the photocatalytic degradation, further illustrating that the hydroxyl radicals acted as active species and were successfully trapped.

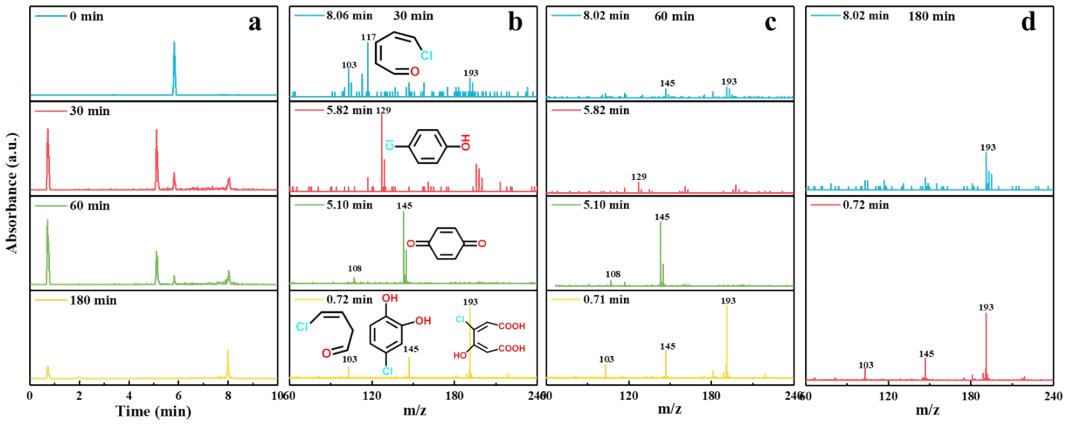

Figure S27 (a) The HPLC chromatograms of 4-chlorophenol at different degradation periods, (b), (c), and (d) correspond to the mass spectra of the intermediate products in the photocatalysis-self-Fenton system degradation of 4-chlorophenol for 30 min, 60 min, and 180 min, respectively.

Table S4 The comparison of the degradation activities for organic pollutants in the reported literature

Photocatalyst	Reaction type	Organic Pollutants	Catalyst dose	H_2O_2	Light source	Activity	TOC removal	Ref.
C-Boron/Fe(III)	Fenton	DEP (20 mM)	NA	0.5 mM (additional)	NA	100%/25 min (0.46 min^{-1})	NA	[57]
FeS/Fe(II)	Fenton	Phenol (5 ppm)	3 g/L	0.5 mM (additional)	NA	35%/120 min (Na)	NA	S[1]
$CoFe_2O_4/MoS_2$	Fenton	Phenol (20 ppm)	30 mg	500 μL (additional)	NA	>70%/25 min (NA)	NA	S[2]
Fe_xO_y-d-g-C_3N_4	Fenton	BPA (20 PPM)	1.0 g/L	10 mM (additional)	NA	97.3%/120 min (NA)	35.3% (60 min)	S[3]
g-C_3N_4-MgO	Fenton	SMX (20 ppm)	0.2 g/L	0.03% (additional)	NA	93%/300 min (NA)	NA	S[4]
Nano-SCH	Fenton	4-NP (10 ppm)	0.2 g/L	3 mM (additional)	NA	91%/60 min (0.074 min^{-1})	34.3% (60 min)	S[5]
10 ppm Fe^{2+}	Photo-Fenton	Phenol (1000 ppm)	10 ppm	NA	50℃ with UV-Vis	NA	~80%/180 min	S[6]
Fe-KIT(6)	Photo-Fenton	LA (30 ppm)	1.0 g/L	24 mM (additional)	UV-Vis (ACTINIC BL20)	98%/240 min (NA)	44.75%	S[7]
Fe_2O_3-SiO_2	Photo-Fenton	MO (20 ppm)	1.0 g/L	0.4 mM (additional)	100 W Hg lamp (λ>420 nm)	97%/30 min (NA)	NA	S[8]
AG/Fe_3O_4	Photo-Fenton	Phenol (0.4 mM)	0.5 g/L	150 mM (additional)	Sunlight	92.4%/120 min (NA)	NA	S[9]
Hematite nanoparticles	Photo-Fenton	RhB (20 μM)	1.0 g/L	0.1 M (additional)	200 W Xe lamp	NA (0.0022 min^{-1})	26.59% (420 min)	S[10]
FeOOH/g-C_3N_4	Photo-Fenton	Phenol (50 ppm)	4.0 g/L	30 μL (additional)	500 W Xe lamp (λ>420 nm)	100%/90 min (0.054 min^{-1})	74% (120 min)	S[11]
Fe_2O_3/CuO/MCM41	Photo-Fenton	MB (10 ppm)	1.0 g/L	300 μL (additional)	500 W Xe lamp (λ>420 nm)	99.45%/45 min (NA)	NA	S[12]
Mn-doped MIL-88B-Fe	Photo-Fenton	Phenol (50 ppm)	0.1 g/L	1 mL (additional)	300 W Xe (AM 1.5)	96%/120 min (NA)	NA	S[13]
HSO_3-MIL-53(Fe)	Photo-Fenton	CBZ (10 ppm)	0.2 g/L	100 μL (additional)	500 W Xe lamp (λ>420 nm)	100%/90 min (0.064 min^{-1})	30% (90 min)	S[14]
$Zn_{1-1.5x}Fe_xS$/g-C_3N_4	Photo-Fenton	NPN (10 ppm)	1.0 g/L	3 mM (additional)	500 W Xe lamp (Simulated solar)	90.7%/60 min (2.436 h^{-1})	55.4 % (60 min)	S[15]
a-Fe_2O_3/g-C_3N_4	Photo-Fenton	TC-H (10 ppm)	1.0 g/L	NA	300 W Xe lamp	95%/150 min (1.2 h^{-1})	86% (180 min)	S[16]
g-C_3N_4/PDI/Fe	Photo-Fenton	BA (10 ppm)	1.0 g/L	NA	300 W Xe lamp (λ>420 nm)	100%/180 min	NA	S[17]
g-C_3N_4	Photocatalytic	Phenol (10 ppm)	1.0 g/L	NA	300 W Xe lamp (λ>400 nm)	90%/180 min (0.57 h^{-1})	NA	S[18]
Fe_2O_3QDs/2D-C_3N_4	Photocatalytic	MB (10 ppm)	0.3 g/L	NA	300 W Xe lamp	75%/180 min (0.472 h^{-1})	NA	S[19]
Ag/Fe_3O_4/g-C_3N_4	Photocatalytic	TC (20 ppm)	0.5 g/L	NA	300 W Xe lamp (λ>420 nm)	88%/90 min (1.308 $h^{-1)}$	NA	S[20]
a-FeOOH/CNNS	Photocatalytic	RhB (10 ppm)	1.0 g/L	NA	500 W Xe lamp	95%/240 min (0.642 h^{-1})	NA	S[21]

					(λ≥420 nm)			
NiFe-LDH/N-rGO/g-C_3N_4	Photocatalytic	RhB (20 ppm)	1.0 g/L	NA	Sun Light	97%/120 min (1.044 h^{-1})	NA	S[22]
GQDs/g-CNNR	Photocatalytic	OTC (15 ppm)	1 g/L	NA	300 W Xe lamp (λ>420 nm)	80%/120 min (NA)	68.1 % (120 min)	S[23]
GO/PI	Photocatalytic	2,4-DCP (10 ppm)	1 g/L	NA	300 W Xe lamp (λ>420 nm)	95%/120 min (0.024 min^{-1})	52.0 % (120 min)	S[24]
PI-g-C_3N_4	Photocatalytic	BPA (10 ppm)	1.0 g/L	NA	300 W Xe lamp (λ>400 nm)	96%/60 min (3.01 h^{-1})	54% (60 min)	S[25]
FeOCl/CDots	photo-assisted Fenton	4-CP (5 ppm)	1.0 g/L	337.2 μM (180 min) (during degradation)	150 W Xe lamp (λ>420 nm)	90.1%/180 min (0.72 h^{-1})	NA	S[26]
OPCN	Photocatalysis-self-Fenton	2, 4-DCP (5 ppm)	0.5 g/L	50.12 μM (120 min) (during degradation)	10 W LED Light (λ>420 nm)	98.4%/60 min (4.14 h^{-1})	42.22% (120 min)	[37]
P-g-C_3N_4	Photocatalysis-self-Fenton	2, 4-DCP (20 ppm)	1.0 g/L	70.5μM (180 min) (during degradation)	500 W metal-halide-lamp (λ>420 nm)	92%/180 min (0.82 h^{-1})	42.7 % (180 min)	[38]
Cg-C_3N_4	Photocatalysis-self-Fenton	4-CP (20 ppm)	0.4 g/L	173.8μM (120 min) (during degradation)	300 W Xe lamp (λ>420 nm)	97.3%/120 min (1.733 h^{-1})	59.6 % (180 min)	This work

References

1. D. Cheng, A. Neumann, S. Yuan, W. Liao, A. Qian, *Environ. Sci. Technol*., 2020, **54**, 4091-4101.

2 Q. Yan, C. Lian, K. Huang, L. Liang, H. Yu, P. Yin, J. Zhang, M. Xing, *Angew. Chem. Int. Ed. Engl*, 2021, **60**, 17155-17163.

3. Y. Wang, P. Zhang, T. Li, L. Lyu, Y. Gao, C. Hu, *J. Hazard Mater*., 2021, **408**, 124818.

4. T. Li, L. Ge, X. Peng, W. Wang, W. Zhang, *Water Res*., 2021, **190**, 116777.

5. X. X. Qiao, K. Yu, J.Y. Xu, Y.L. Cai, Y.F. Li, H.L. Cao, J. Lü, *Appl. Surf. Sci*., 2021, **548**, 149248.

6. J. Carbajo, J.E. Silveira, G. Pliego, J.A. Zazo, J.A. Casas, *Sep. Purif. Technol*., 2021, **271**, 118876.

7. T.B. Benzaquen, D.A. Barrera, P.M. Carraro, K. Sapag, O.M. Alfano, G.A. Eimer, *Environ. Sci. Pollut. Res. Int*., 2019, **26** (5) (2019) 4192-4201.

8. L. Zhou, J. Lei, L. Wang, Y. Liu, J. Zhang, *Appl. Catal. B: Environ*., 2018, **237**, 1160-1167.

9. P.K. Boruah, B. Sharma, I. Karbhal, M.V. Shelke, M.R. Das, *J. Hazard Mater*., 2017, **325**, 90-100.

10. X. Huang, Y. Chen, E. Walter, M. Zong, Y. Wang, X. Zhang, O. Qafoku, Z. Wang, K.M. Rosso, *Environ. Sci. Technol*., 2019, **53**, 10197-10207.

11. X. Qian, Y. Wu, M. Kan, M. Fang, D. Yue, J. Zeng, Y. Zhao, *Appl. Catal. B: Environ*., 2018, **237**, 513-520.

12. T. Sun, M. Gong, Y. Cai, S. Xiao, L. Zhang, Y. Zhang, Z. Xu, D. Zhang, Y. Liu, C. Zhou, *Res. Chem. Intermed*., 2019, **46**, 459-474.

13. J. Ding, Y.G. Sun, Y.L. Ma, *ACS Omega*., 2021, **6**, 2949-2955.

14. S. Sun, Y. Hu, M. Xu, F. Cheng, H. Zhang, Z. Li, *J. Hazard Mater*., 2022, **424**, 127698.

15. Q. Wang, P. Wang, P. Xu, Y. Li, J. Duan, G. Zhang, L. Hu, X. Wang, W. Zhang, *Appl. Catal. B: Environ*., 2020, **266**, 118653.

16. Y. Wang, H. Song, J. Chen, S. Chai, L. Shi, C. Chen, Y. Wang, C. He, *Appl. Surf. Sci*., 2020, **512**, 145650.

17. Z. Xiong, Y. Zhang, *Environ. Res*., 2021, **195**, 110785.

18. H. Zhang, L.H. Guo, L. Zhao, B. Wan, Y. Yang, *J. Phys. Chem. Lett*., 2015, **6**, 958-63.

19. Q. Hao, Z. Mo, Z. Chen, X. She, Y. Xu, Y. Song, H. Ji, X. Wu, S. Yuan, H. Xu, H. Li, *Colloid. Surfaces A*, 2018, **541**, 188-194.

20. Z. Zhu, Z. Lu, D. Wang, X. Tang, Y. Yan, W. Shi, Y. Wang, N. Gao, X. Yao, H. Dong, *Appl. Catal. B: Environ*., 2016, **182**, 115-122.

21. H. Yang, S. Zhang, R. Cao, X. Deng, Z. Li, X. Xu, *Sci. Rep*., 2017, **7**, 8686.

22. S. Nayak, K.M. Parida, *Sci. Rep*., 2019, **9**, 2458.

23. A. Yuan, H. Lei, F. Xi, J. Liu, L. Qin, Z. Chen, X. Dong, *J. Colloid Interface Sci*., 2019, **548**, 56-65.

24. Y. Gong, B. Yang, H. Zhang, X. Zhao, C. Zhu, *Mater. Res. Bull*., 2019, **112**, 115-123.

25. J. Zhang, X. Zhao, Y. Wang, Y. Gong, D. Cao, M. Qiao, *Appl. Catal. B: Environ*., 2018, **237**, 976-985.

26. J. Zhang, G. Zhang, Q. Ji, H. Lan, J. Qu, H. Liu, *Appl. Catal. B: Environ*., 2020, **266**, 118665.

27. T. Kanata-Kito, M. Matsunaga, H. Takakura, Y. Hamakawa, T. Nishino, *Proc. SPIE*, 1990, **1286**, 56-66.

28. J. S. Im, H. Kollmer, J. Off, A. Sohmer, F. Scholz, A. Hangleiter, *Phys. Rev. B*, 1998, **57**, R9435.

29. P. Lefebvre, J. Allègre, B. Gil, H. Mathieu, N. Grandjean, M. Leroux, J. Massies, P. Bigenwald, *Phys. Rev. B*, 1999, 59, 15363-67.
30 G. Morello, F. D. Sala, L. Carbone, L. Manna, G. Maruccio, R. Cingolani, M. D. Giorgi, *Phys. Rev. B*, 2008, **78**, 195313.
31. F. Le Formal, K. Sivula, M. Grätzel, *J. Phys. Chem. C*, 2012, **51**, 26707–26720.
32. J. Li, L. J. Cai, J. Shang, Y. Yu, L. Z. Zhang, *Adv. Mater*., 2016, **21**, 4059-4064.
33. J. Li, G. M. Zhan, Y. Yu, L. Z. Zhang, *Nat. Commun*., 2016, **11480**, 1-9.